

Array-Level Inverse Design of Beam Steering Active Metasurfaces

Prachi Thureja,[§] Ghazaleh Kafaie Shirmanesh,[§] Katherine T. Fountaine, Ruzan Sokhoyan, Meir Grajower, and Harry A. Atwater*



Cite This: <https://dx.doi.org/10.1021/acsnano.0c05026>



Read Online

ACCESS |



Metrics & More



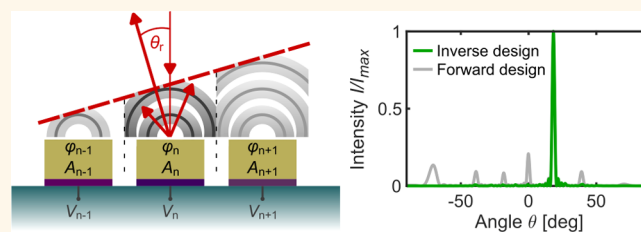
Article Recommendations



Supporting Information

ABSTRACT: We report an array-level inverse design approach to optimize the beam steering performance of active metasurfaces, thus overcoming the limitations posed by nonideal metasurface phase and amplitude tuning. In contrast to device-level topology optimization of passive metasurfaces, the outlined system-level optimization framework relies on the electrical tunability of geometrically identical nanoantennas, enabling the design of active antenna arrays with variable spatial phase and amplitude profiles. Based on this method, we demonstrate high-directivity, continuous beam steering up to 70° for phased arrays with realistic tunable antenna designs, despite nonidealities such as strong covariation of scattered light amplitude with phase. Nonintuitive array phase and amplitude profiles further facilitate beam steering with a phase modulation range as low as 180° . Furthermore, we use the device geometries presented in this work for experimental validation of the system-level inverse design approach of active beam steering metasurfaces. The proposed method offers a framework to optimize nanophotonic structures at the array level that is potentially applicable to a wide variety of objective functions and actively tunable metasurface antenna array platforms.

KEYWORDS: *inverse design, active metasurface, phased array, beam steering, array configuration, genetic algorithm, wavefront engineering*



Optical beam steering has recently been the subject of intensive worldwide research, owing to its importance for technology applications such as light detection and ranging (LiDAR), free space optical communications, and holographic displays.^{1–4} Operation at near-infrared (NIR) and visible wavelengths has the potential to enable high-resolution beam steering arrays with reduced footprints. Wave front shaping relies on the control of phase and amplitude over antennas in an emitting array. Interference of light scattered from each antenna in an array gives rise to radiated wave fronts emanating from the array which can be tailored to create a desired far-field intensity profile. Conventional optical phased arrays (OPAs) alter the phase and amplitude of an input guided wave using phase shifters that are typically based on thermo-optic^{4–6} or microelectromechanical systems (MEMS).^{7–9} However, large thermal time constants limit scanning frequencies while high mechanical failure rates reduce device reliability. Alternative approaches employing p-i-n diodes have been demonstrated for high modulation frequencies of up to 200 MHz.¹⁰ Nevertheless, the spatial arrangement of waveguides in arrays typically demands large interantenna spacings to avoid crosstalk between adjacent elements.^{11,12} In the case of equidistantly spaced elements, this limits the grating lobe-free steering range. Researchers have demonstrated beam steering with large field of view (FOV)

using nonuniform antenna arrangements in sparse arrays,^{12,13} yet considerable amounts of background noise are reported in the far-field radiation patterns.

Planar metasurfaces offer an ideal platform to address the challenges stated above. Metasurfaces are compact arrangements of nanostructured resonators arrayed at a subwavelength spacing, enabling the realization of beam steering devices with enhanced FOV. The resonances of individual metasurface antennas impart local changes to the scattered light phase and amplitude. Anomalous reflection has previously been reported using passive metasurfaces^{3,14–18} that consist of a set of precisely designed antenna elements that are fixed at the time of fabrication. To achieve this, phased arrays are designed as periodic arrangements of antennas that generate a blazed grating-like array profile with constant phase increments between adjacent elements. Such arrays have been designed by researchers using a “forward” design process, motivated by

Received: June 16, 2020

Accepted: October 6, 2020



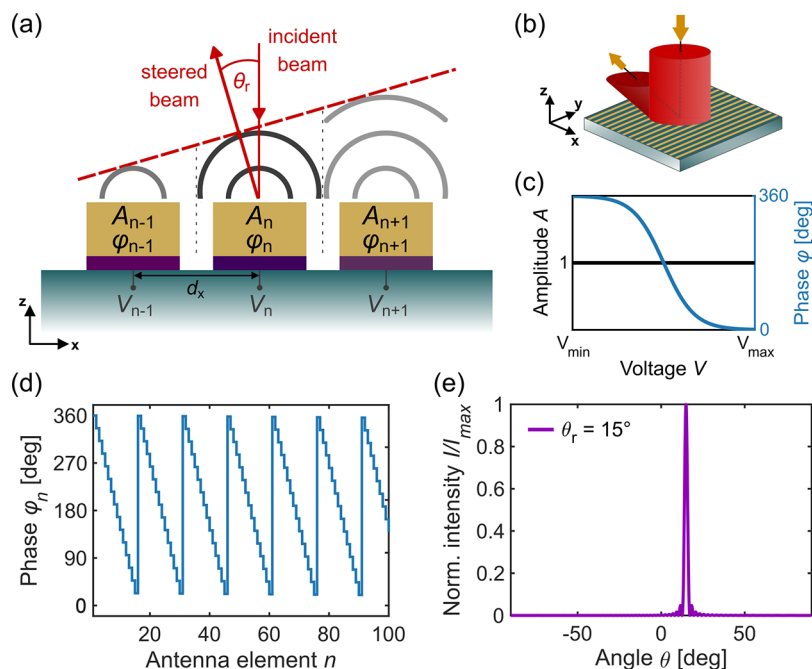


Figure 1. (a) Schematic of beam steering active metasurface: application of voltage stimulus V_n on antenna n (yellow) alters the complex dielectric permittivity of the active layer indicated in shades of violet. As a consequence, the scattered light amplitude and phase of element n , A_n , and φ_n , respectively, are varied. The antennas are uniformly arranged at a period d_x . We consider a reflectarray with incident light normal to the surface. Beam steering is achieved by constructive interference of the scattered light at the desired steering angle θ_r . (b) Schematic of a one-dimensional tunable metasurface. Antennas are connected in y -direction and allow independent control in x . (c) Representative scattered light amplitude and phase response of an ideal active antenna array. A phase shift of 360° is achieved for applied bias voltages ranging from V_{\min} to V_{\max} . A constant unit amplitude accompanying the smooth phase shift additionally enables high beam steering performances. (d) Forward design of blazed grating for an ideal phased array consisting of 100 antennas arranged at a period of $d_x = 400$ nm. The operating wavelength is $\lambda = 1550$ nm and the target steering angle is $\theta_r = 15^\circ$. (e) Normalized far-field intensity I/I_{\max} vs polar angle θ for forward design of ideal phased array. The corresponding directivity at $\theta_r = 15^\circ$ is $D_{\text{ideal}} = 78.2$.

principles derived from beam steering with conventional phased arrays at radio frequencies (RF)^{19–21} and spatial light modulators at optical frequencies.²² Passive metasurfaces, however, do not allow for postfabrication tunability. This limits the beam steering function of such devices to a single, design-specific angle.

Recently, considerable effort has been devoted to the design of active metasurfaces that enable temporal modulation of the scattered light amplitude and phase.²³ Active control is achieved by employing antenna structures that—in comparison to passive metasurfaces—consist of an additional tunable permittivity component that is integrated into the metasurface unit cell (Figure 1a). When this active layer is actuated by an external stimulus, such as an electrical bias,^{24–30} thermal heating,^{31,32} or mechanical actuation,^{33–35} it locally and dynamically alters the refractive index of individual unit cells. This approach renders optical frequency metasurfaces to be reconfigurable, with a wide range of phase and amplitude values, in principle similar to RF phased arrays. However, it is much more challenging to temporally modulate optical phase and amplitude since the bandwidth of electronics is too low to allow direct temporal modulation at signal frequencies approaching the optical carrier frequency. Thus, metasurface modulation mechanisms at optical frequencies generally rely on intrinsic resonances that locally modulate the permittivity of a resonant antenna structure. This introduces nonidealities in the optical response. In contrast to passive structures, active metasurfaces often exhibit a strongly covarying phase and amplitude as a function of the applied bias. In addition, it is

challenging to design tunable-permittivity antennas with a full phase modulation range of 360° .^{27,36} As a consequence, active beam steering metasurfaces with forward-designed array phase profiles result in decreased directivities, as nonidealities in the scattered light characteristics result in coupling of significant power into undesired sidelobes.³⁰

Here, we introduce an array-level “inverse” design as a solution to optimize antenna amplitude and phase across an array. Previously, inverse design techniques have mostly been applied to shape and topology optimization of individual nanophotonic components, such as antennas in passive metasurfaces.^{37–42} The shape and size of each nanoantenna evolve over multiple iterations until a specified scattered light response is obtained. Various methods have successfully been demonstrated for this purpose, including the adjoint variable method,^{38,43} genetic algorithms,^{41,44} and machine learning.^{43,45,46} An analogous approach that is most useful for the optimization of active metasurfaces would begin with the design of an array of geometrically identical nanoantennas that exhibit optimal phase and amplitude tunability as a function of an external control variable. Thus, the critical component-level inverse design objective is not shape optimization of a passive metasurface element, but shifts to the design of nanoantennas with optimal functional characteristics, such as the range of achievable amplitude, phase or polarization values in response to its inputs. Finally, once an optimal active antenna design is developed, the co-optimization of the scattering properties of the entire array of antennas enables achieving a desired array performance objective. Due to the additional layer of

complexity, inverse design of active metasurfaces has remained largely unexplored until recently.

Chung *et al.*⁴⁷ recently demonstrated inverse design of an active beam switching metasurface. Notably, the metasurface based on a liquid crystal platform operated in only two states: voltage on and off. As a consequence, topology optimization of individual unit cells was required to facilitate beam switching between different diffraction orders. In contrast, the array-level inverse design approach outlined in this work exploits the tunability of individual active nanoantennas that is made possible by the application of an independent bias to each metasurface antenna.^{30,48} This method results in an array of active antennas each with continuously variable phase and amplitude, yielding a vast number of operation states that allow versatile metasurface function. As a consequence, scattered light phase and amplitude can be optimized across a large array without any change in the geometric configuration of individual components. This concept gives rise to the opportunity for array-level optimization of user-defined metasurface functions, as outlined in this work. Moreover, the proposed array-level inverse design constitutes a critical element for hierarchical codesign of both the entire array and the active antenna element in tunable metasurfaces. This approach ultimately aims to simultaneously optimize the array configuration via the external voltage control variable, the nanoantenna shape, as well as its complex dielectric function for a desired metasurface response.

We utilize a genetic algorithm for an iterative optimization of a figure of merit (FOM) that analytically describes the desired metasurface function. Thus, optimized array phase and amplitude profiles are obtained without the need of a finite-difference time-domain (FDTD) solver. While it is possible to use alternative optimization methods, our analysis illustrates the power of array-level optimization for nanophotonics design. We apply array-level optimization to a beam steering active metasurface with nonideal antenna components exhibiting a limited phase shift and considerable amplitude-phase covariation.³⁰ Iterative optimization generates highly nonintuitive array phase and amplitude profiles that significantly enhance the beam steering performance for a broad range of steering angles, with optimization performed at angular increments of 0.5°. Furthermore, in comparison to forward designs, array-level inverse design enables increased beam steering performance with a phase modulation range as small as 180°. We validate the outlined design approach experimentally by comparing beam steering performances that are obtained using forward- and inverse-designed array profiles in a metasurface exhibiting a phase shift of approximately 220°. Finally, we have performed an analysis of the effect on beam steering of array-level “noise” resulting from phase and amplitude fluctuations from targeted values.

RESULTS AND DISCUSSION

Forward Design in Ideal Antenna Arrays. The electric far-field E_{ff} of an array of scatterers is calculated by pattern multiplication of the electric far-field of a unit cell E_{antenna} with the array factor.^{20,49} The array factor calculation is based on an array of independent scatterers with negligible near-field coupling. The far-field response is thus obtained by applying the Fraunhofer approximation to the superposition of individual electric field contributions from each scattering element. The validity of the independent scatterer model in

metasurfaces with subwavelength spacing is verified in [Supporting Information Part 1](#).

In a one-dimensional configuration, the array factor is computed by taking into account the phase φ_n , amplitude A_n , as well as the period d_x that defines the position of the n th antenna element ([Figure 1a](#)). The scattered light phase and amplitude are determined by the external stimulus applied to each antenna, such as a bias voltage V_n .

$$E_{\text{ff}}(\theta) = E_{\text{antenna}}(\theta) \sum_n [A_n(V_n) \exp(i\varphi_n(V_n)) \exp(ik(n-1)d_x \sin(\theta))] \quad (1)$$

Here, θ is the polar angle, and $k = 2\pi/\lambda$ is the wavenumber associated with the operating wavelength λ . A 1D configuration of a square antenna array is realized by connecting antennas along one axis and enabling independent control of each element in the perpendicular direction ([Figure 1b](#)). In a beam steering reflectarray, the incident light is normal to the metasurface, and the reflected beam is steered at a desired angle θ_r .

We define an ideal antenna response as one that yields a constant unit amplitude and a smoothly varying phase with a 360° phase modulation range ([Figure 1c](#)). The respective ideal amplitude and phase properties are commonly reported in conventional phased array systems⁵ as well as passive metasurfaces.¹⁴ A complete phase modulation in combination with constant amplitudes over the entire antenna array facilitates intuitively understandable forward design of phase gradient profiles for highly directive beam steering with minimal power loss in sidelobes. The additional manifestation of unit amplitude at each nanoantenna results in maximal power efficiency. [Figure 1d](#) illustrates a blazed grating design for an ideal reflectarray consisting of 100 antennas that are uniformly arranged at a spacing of $d_x = 400$ nm. The operating wavelength is $\lambda = 1550$ nm. Discontinuities in the phase profile arise due to the discreteness of the array owing to the finite antenna size (see [Supporting Information Part 2](#)). For constant amplitude, the phase gradient profile shown in [Figure 1d](#) results in a directive beam steered at $\theta_r = 15^\circ$ with minimal power scattered in other directions ([Figure 1e](#)). The far-field radiation pattern is calculated as $I(\theta) = |E_{\text{ff}}(\theta)|^2$. Individual antennas are approximated as omnidirectional scattering elements with $E_{\text{antenna}}(\theta) = 1$. For the purpose of our study, we quantify the beam steering performance by the directivity, that is defined as the ratio between the intensity at the desired angle θ_r to the power radiated in all directions normalized by the solid angle. In contrast to efficiency, directivity remains unaffected by scaling of the far-field radiation pattern by a constant factor. We refer the reader to [Supporting Information Part 3](#) for a discussion on alternative performance metrics for beam steering metasurfaces. For a one-dimensional reflectarray radiating into a half-space, the directivity $D(\theta_r)$ is formalized as²⁰

$$D(\theta_r) = \frac{\pi I(\theta_r)}{\int_{-\pi/2}^{\pi/2} I(\theta) d\theta} \quad (2)$$

For the structure analyzed here, [eq 2](#) yields a directivity of $D_{\text{ideal}} = 78.2$. The sidelobe level SL is proportional to the ratio of the second largest to largest peak intensity, $I_{\text{max},2}$ and $I_{\text{max},1}$ respectively.

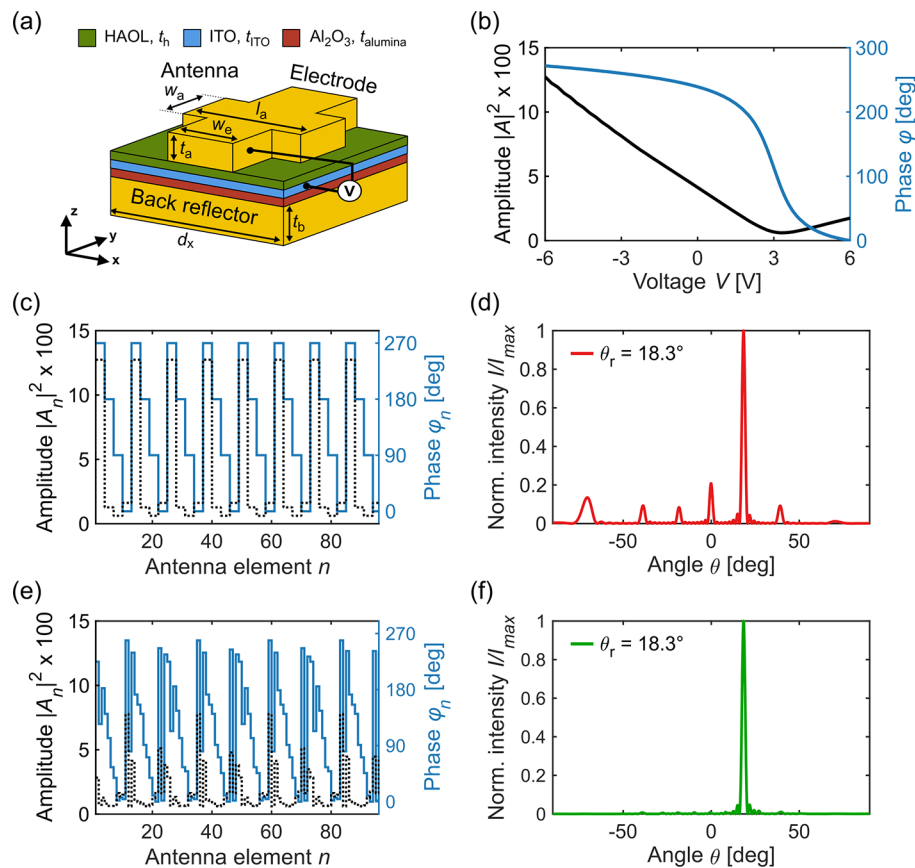


Figure 2. (a) Single unit cell of a plasmonic metasurface as demonstrated in ref 30. Constitutive layers from top to bottom: Au rectangular patch ($t_a = 40$ nm, $w_a = 130$ nm, $l_a = 230$ nm) and electrode ($w_e = 150$ nm), hafnium oxide/aluminum oxide laminated dielectric spacer (HAOL, $t_h = 9.5$ nm), active ITO layer ($t_{\text{ITO}} = 5$ nm), Al_2O_3 dielectric layer ($t_{\text{alumina}} = 9.5$ nm), and Au back reflector ($t_b = 80$ nm). The electrode connects Au patches in y -direction and allows independent control in x -direction by application of an external bias voltage V . The metasurface consists of 96 tunable antennas in x which are periodically arranged at a spacing of $d_x = 400$ nm. (b) Scattered light amplitude (black) and acquired phase (blue) response as a function of the applied bias voltage at a wavelength of $\lambda = 1510$ nm. For clarity, the phase axis is set to 0° at its minimal value. The optical properties are obtained through full-wave simulation (Lumerical FDTD) of a periodic array of the unit cell with a given bias voltage across the entire array. (c) Stairstep phase (blue) and amplitude (black dotted) profile for steering at $\theta_r = 18.3^\circ$. (d) Normalized far-field intensity I/I_{max} as a function of polar angle θ for forward design of nonideal active metasurface. The directivity at $\theta_r = 18.3^\circ$ is $D_{\text{forward}} = 39.5$. (e) Optimized phase profile (blue) with corresponding amplitude profile (black dotted) generated by inverse design for steering at $\theta_r = 18.3^\circ$. (f) Normalized far-field intensity I/I_{max} vs polar angle θ for inverse design of active metasurface. The optimized directivity at $\theta_r = 18.3^\circ$ is $D_{\text{inverse}} = 72.7$.

$$SL = 10 \log_{10} \left(\frac{I_{\text{max},2}}{I_{\text{max}}} \right) \quad (3)$$

For the ideal, forward-designed antenna array shown in Figure 1, the sidelobe level corresponds to $SL_{\text{ideal}} = -13.3$ dB.

Inverse Design of Nonideal Active Metasurfaces. In contrast to ideal phased arrays, active metasurfaces typically exhibit a nonideal optical response due to the device-specific modulation mechanism. Here, we illustrate this behavior using the example of an electro-optically tunable, plasmonic metasurface.³⁰ Figure 2a shows a square unit cell with a characteristic period of $d_x = 400$ nm. It consists of a rectangular gold (Au) patch over a hafnium/aluminum oxide laminated (HAOL) gate dielectric and an active indium tin oxide (ITO) layer. This composite structure is deposited on top of an Al_2O_3 dielectric spacer and an Au back reflector. Au electrodes intersecting the top metal patches in the y -direction enable the formation of equipotential rows, analogous to Figure 1b. The entire metasurface consists of 96 independently addressable rows, referred to as metasurface antennas.

Active control is achieved by employing field-effect induced changes in refractive index to manipulate the scattered light properties.^{50,51} The Au-HAOL-ITO heterostructure acts like a metal-oxide-semiconductor (MOS) capacitor. Application of an electrical bias between the Au electrode and the ITO layer introduces a carrier density modulation in the ITO. Thus, a change in the complex dielectric permittivity of the ITO, ϵ_{ITO} , occurs in a thin layer at the interface to the gate dielectric.²⁷ Upon alteration of the applied electric field, $\text{Re}(\epsilon_{\text{ITO}})$ switches its sign from positive to negative, enabling operation in an epsilon-near-zero (ENZ) regime. Due to the continuity of the normal electric displacement component, the ENZ condition imposes a strong field enhancement in the active layer.²⁴ Spectral overlap of the ENZ transition with the magnetic dipole resonance of the antenna ensures a strong modulation of the scattered light response, allowing for effective device operation at telecommunication wavelengths. We note here that while $\text{Re}(\epsilon_{\text{ITO}})$ is required to go to zero to satisfy the ENZ condition and ensure a large phase modulation, $\text{Im}(\epsilon_{\text{ITO}})$ takes nonzero values, as shown in Supporting Information Part 4. The losses emerging from absorption in the active layer due to

electron–electron collisions⁵² result in reduced scattered light amplitudes.

Figure 2b shows the reflectance and acquired phase properties of this active metasurface simulated at $\lambda = 1510$ nm. The operation wavelength is chosen so as to give rise to large phase modulation with a modest change in amplitude.³⁰ Nevertheless, the device exhibits a nonideal optical response with (i) a nonunity amplitude, (ii) a limited phase modulation range of 272° , and (iii) covariation of the scattered light amplitude and phase properties with applied bias. These nonidealities significantly limit the beam steering performance of such a metasurface array designed using a forward approach, in the following ways: First, reduced phase modulation requires adjustment to ideal blazed grating designs. Stairstep phase profiles approximate the spatial phase gradients as shown in Figure 2c.³⁰ A dynamic change of the repetition number (*i.e.*, number of adjacent antennas with the same phase value) results in beam steering at a set of discrete angles. However, reduced phase modulation introduces more sidelobes in the far-field radiation pattern (see Supporting Information Part 5). Moreover, the additional covariance of the scattered light amplitude and phase rules out the design of pure phase gratings. Since an intuition-based forward design does not account for amplitude-phase covariation, substantial power is coupled into undesired sidelobes, as shown in Figure 2d for steering at an angle of $\theta_r = 18.3^\circ$. As a result of these nonidealities, we observe a significant drop in directivity to $D_{\text{forward}} = 39.5$. The corresponding sidelobe level is $SL_{\text{forward}} = -6.8$ dB. These limitations pose an inherent challenge on the design of active metasurfaces and demand an alternative approach to facilitate high performance beam steering metasurfaces with nonideal antennas.

Here, we report an array-level inverse design algorithm that computes the bias voltage configuration for an electrically tunable metasurface to achieve optimized beam steering. Since each metasurface antenna is gated individually, the algorithm aims to optimize the covarying phase and amplitude value at each antenna. We address this multiparameter, global optimization problem using genetic algorithms (GA). In contrast to local search methods, genetic algorithms are based on stochastic optimizers that can escape local optima.^{53,54} In addition, they are highly suitable for discrete solution domains with discontinuous or nondifferentiable objective functions.⁴¹ An inherently high-dimensional solution space arises due to simultaneous optimization of 96 metasurface antennas. This challenge is overcome by implementing an iterative genetic optimization that relies on a gradual increase of the solution space. The algorithm initially runs an optimization for a reduced number of consecutive antennas, which are periodically repeated over the entire array. Once an optimal solution is found, it is passed on to the next bigger solution domain as an initial solution. The final iteration simultaneously optimizes all variables (see Supporting Information Part 6 for the numerical framework of the iterative optimization). This approach enables the algorithm to effectively find near-optimal solutions in high-dimensional optimization spaces, while maintaining all degrees of freedom. Due to the stochastic nature of genetic optimization, the algorithm is implemented over multiple rounds to obtain the optimal result in an extended data set. Further details regarding the distribution and robustness of the optimized results, as well as a comparison to the direct noniterative optimization of 96 antennas are provided in Supporting Information Part 7. We

would like to highlight that due to the high dimensionality of the nonconvex solution space given in this problem, the search for an absolute global optimum becomes infeasible. Thus, we compare the optimized FOM to the corresponding performance measure of an ideal antenna array in order to assess its proximity to a desired reference value.

The beam steering optimization consists of maximizing the directivity at the desired steering angle θ_r . Thus, the objective function is defined as

$$\text{FOM}(\theta_r, q_n(V_n), A_n(V_n)) = D(\theta_r) \quad (4)$$

The directivity accounts for the antenna-specific control variables (in this case, bias voltage) to maximize the intensity at θ_r , while minimizing power scattered in all other directions. The latter also simultaneously minimizes the beam divergence, which is quantified by the full width at half-maximum (FWHM) of the steered beam. The inverse design algorithm outputs a highly nonintuitive array phase profile, as shown in Figure 2e for the same steering angle of $\theta_r = 18.3^\circ$. The seemingly periodic nature of the spatial phase profile arises from the phase gradient required to steer a beam at a specified angle as well as the iterative design approach. Since the inverse design optimizes the covarying phase and amplitude values at each antenna, the algorithm aims to minimize the amplitude modulation A_{mod} over the entire antenna array.

$$A_{\text{mod}} = \frac{|A_{\text{max}}|^2 - |A_{\text{min}}|^2}{|A_{\text{min}}|^2} \quad (5)$$

Here, A_{max} and A_{min} correspond to the maximal and minimal amplitudes, respectively. The amplitude modulation for the forward-designed array profile (Figure 2c) corresponds to $A_{\text{mod,forward}} = 19.7$. In comparison, the amplitude modulation using the inverse design approach (Figure 2e) is $A_{\text{mod,inverse}} = 11.8$. As a result, by accounting for the antenna-specific scattered light properties, the co-optimization of phase and amplitude of each antenna results in significant sidelobe suppression, as shown in Figure 2f. The optimized directivity for steering at $\theta_r = 18.3^\circ$ is $D_{\text{inverse}} = 72.7$, representing a substantial increase of 84% compared to the previously demonstrated forward design with $D_{\text{forward}} = 39.5$. Similarly, the sidelobe level obtained through inverse design amounts to $SL_{\text{inverse}} = -13.2$ dB.

These findings highlight the ability of the optimized radiation patterns to approach ideal beam steering. The approach was further generalized to the case of continuous beam steering at angular increments of 0.5° . Figure 3a shows a comparison of the directivity values obtained with forward and inverse design, respectively. In addition to the stairstep profiles discussed in Figure 2, we demonstrate the performance for linear phase profiles that are truncated symmetrically to remain within the respective phase modulation range (see Supporting Information Part 5). This method offers an alternative approach to achieve continuous beam steering using forward design. A cosine-like decrease in directivity is seen for increased steering angles. To understand this phenomenon, we remind ourselves that the two limiting factors defining the beam directivity are the magnitude of the sidelobes relative to the peak intensity at θ_r (*i.e.*, the sidelobe level SL), as well as the FWHM of the main lobe. Notably, the prior does not change monotonically as the beam is scanned over the half space and instead fluctuates around a constant value (inset of Figure 3b). Thus, the decrease in directivity is attributed to the

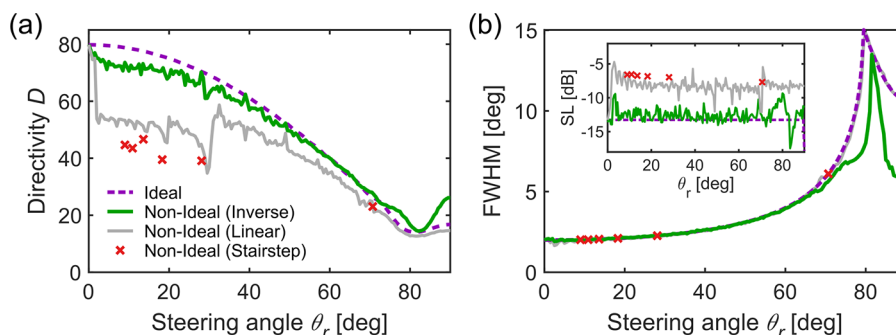


Figure 3. (a) Optimized directivity (green) for beam steering angles θ_r ranging from 0° to 90° at angular increments of 0.5° . The results are obtained for the active metasurface as introduced in Figure 2. The optimized performance approaches ideal beam directivity (dashed violet) at all steering angles. The directivity of forward designs consisting of linear, truncated (gray), or stairstep (red crossed) phase profiles are shown as comparison. (b) Beam divergence (FWHM) as a function of steering angle θ_r for the active metasurface with an aperture of $38.4 \mu\text{m}$. Inset: Sidelobe level (SL) as a function of steering angle θ_r . All values are computed with the assumption of omnidirectional antennas ($E_{\text{antenna}} = 1$).

diminished effect of aperture size at oblique angles. That is, the antenna array aperture appears to be reduced in size at larger steering angles, leading to a broadening of the beam, as illustrated in Figure 3b. Furthermore, since the reflectarray configuration does not allow for radiation to go beyond 90° , the main lobe is truncated for angles greater than 80° . Thus, an increase in directivity and a simultaneous decrease in FWHM is reported for the corresponding steering range. We provide an analysis on the impact of aperture size on the beam directivity in Part 8 of the Supporting Information. Figure 3a highlights the ability of the optimized designs in a nonideal antenna array to approach the performance of an ideal phased array (dashed) at all steering angles. This contrasts with the results of forward design using linear or stairstep phase profiles which reduce performance since they do not account for the nonideal optical response.

An evaluation of the absolute differences between the actual and target steering angle shows that the target angle is achieved with $\leq 0.2^\circ$ absolute deviation for steering angles up to 70° . For broadside angles, this value increases as steering in nonuniform angular increments is observed due to the limited phase modulation (see Supporting Information Part 9). Additional constraints can be implemented in the algorithm to improve the accuracy of the steered beam even at steering angles beyond 70° . Nonetheless, due to a substantial reduction in the FWHM at broadside angles (Figure 3b), optimized directivity values are able to surpass the predicted performance for ideal antenna arrays.

Impact of Phase and Amplitude Modulation. A seemingly fundamental drawback of active metasurfaces is access to a limited phase modulation range $\Delta\phi = \phi_{\text{max}} - \phi_{\text{min}}$. In addition, for the active metasurface discussed above, Figure 2b illustrates that the maximal phase shift of 272° is achieved by a bias application of ± 6 V. Since these levels approach values that are marginal to the breakdown field in the active ITO layer, it is desirable to operate at lower voltage and therefore a lower phase modulation range to increase device lifetime. Thus, for the purpose of this study, we limit the applied bias range to ± 4.5 V in the modeled active metasurface.³⁰ For further reduction in $\Delta\phi$, the phase modulation is truncated symmetrically around the ENZ permittivity transition at 2.75 V. This simultaneously also ensures minimal amplitude modulation A_{mod} which is desirable for enhanced performance.

Figure 4 illustrates the effect of reduced $\Delta\phi$ for this electro-optically tunable metasurface on the performance of forward- and inverse-designed arrays steering at $\theta_r = 18.3^\circ$. The underlying design principle of forward-designed arrays with stairstep phase profiles does not account for the covariation of phase with amplitude. Thus, decreased phase modulation ranges $\Delta\phi$ lead to significant power coupling into undesired sidelobes, as illustrated in the right column of Figure 4 (gray). In contrast, our results indicate that inverse design facilitates highly directive beams even with a limited phase modulation range of merely 210° where directivity is enhanced by up to 55% compared to the respective stairstep forward design (Figure 4d). As the phase modulation range is further reduced, a decrease in the optimized directivity is observed, with increasing sidelobe amplitude at 0° and $-\theta_r$ (Figure 4f,h). Nonetheless, the optimized directivity reported with $\Delta\phi = 150^\circ$ (Figure 4h) is 41% higher than the corresponding forward design and comparable to the directivity of the stairstep phase profile introduced with $\Delta\phi = 270^\circ$ in Figure 2d. This result underscores the ability of the inverse design to create high-performing arrays despite covarying phase and amplitude. However, it does not allow for any decoupled conclusions on the independent effects of phase and amplitude modulation on the optimized performance. Hence, to analyze the significance of limiting the phase modulation range, we studied a series of hypothetical arrays with limited phase modulation, where amplitude was held at a constant value $A = 1$. In addition, we artificially generated representative trial values of the amplitude-voltage relation with modest amplitude modulation where the phase modulation range was held at a constant value of $\Delta\phi = 360^\circ$. For generality, the arrays considered here consist of 100 antennas spaced at a period of 400 nm, with an operating wavelength of 1550 nm.

Figure 5a demonstrates the optimized directivities for active metasurfaces with constant, unit amplitude and varying phase modulation range $\Delta\phi$. Phase is assumed to be a sigmoidal function of the applied bias (see Supporting Information Part 10). As $\Delta\phi$ is reduced, directivity is maintained up to a threshold phase modulation range $\Delta\phi_{\text{threshold}}$. With further distortion in the information carried by each phase element, destructive interference results in intensified sidelobes that reduce directivity. We define $\Delta\phi_{\text{threshold}}$ as the phase modulation range required to obtain the threshold directivity of $0.9 \times D_{\text{ideal}}(\theta_r)$, where $D_{\text{ideal}}(\theta_r)$ corresponds to the

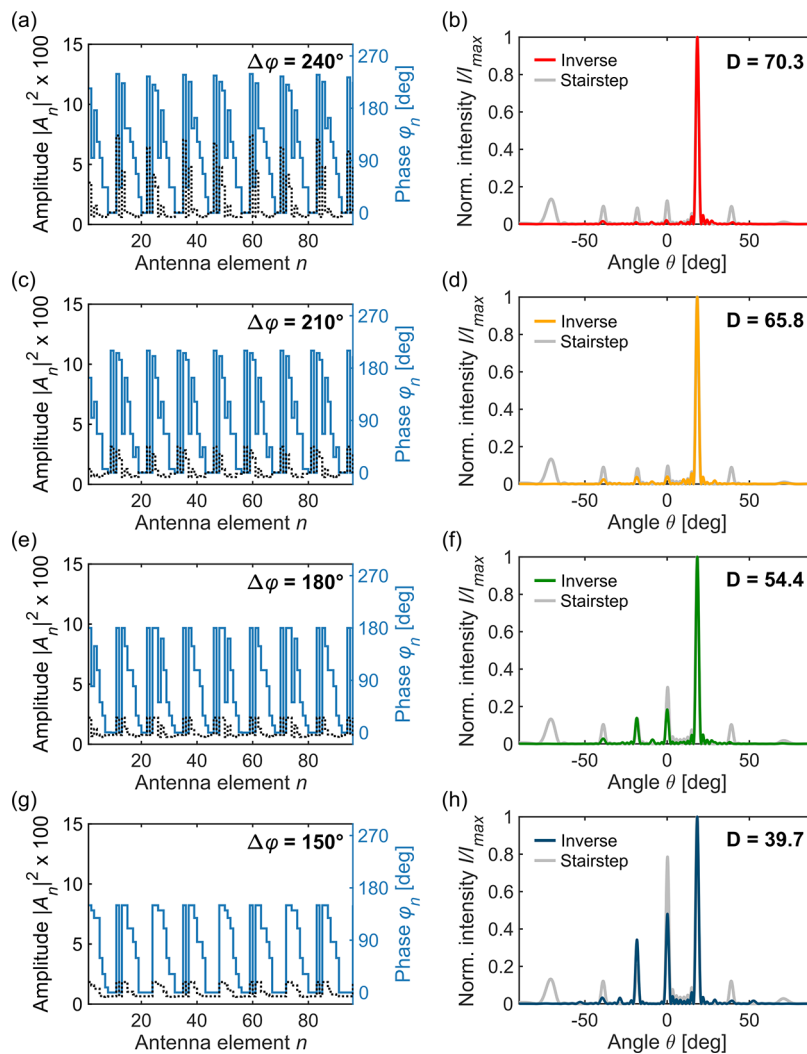


Figure 4. Optimized phase and amplitude designs for steering at $\theta_r = 18.3^\circ$ with reduced phase modulation ranges $\Delta\varphi$ of (a) 240° , (c) 210° , (e) 180° , and (g) 150° for the active metasurface shown in Figure 2. Bias voltages are limited to ± 4.5 V to stay away from the breakdown voltage of ITO. In addition, the phase modulation is truncated symmetrically around the ENZ transition which occurs at a bias voltage of 2.75 V. Panels (b), (d), (f), and (h) illustrate the normalized far-field intensity I/I_{\max} as a function of the polar angle θ for the inverse-designed array phase and amplitude profiles as well as the forward-designed staircase phase profile (gray). The optimized directivity with reduced $\Delta\varphi$ is labeled in the upper right corner of the figure.

directivity of an ideal, forward-designed antenna array. Figure 5b compares $\Delta\varphi_{\text{threshold}}$ for forward-designed antenna arrays with linear truncated phase profiles to those of the corresponding inverse designs. Our results indicate that inverse design lowers the required phase modulation range to obtain threshold performance by a considerable amount. By introducing disorder into the phase profile, the inverse design succeeds in suppressing power coupled into undesired directions. Thus, the inverse design approach outperforms intuitively motivated forward design for reduced phase modulation range. The difference in $\Delta\varphi_{\text{threshold}}$ becomes particularly noticeable at large steering angles due to an additional reduction of the FWHM, as discussed in Figure 3b.

In contrast, we consider antenna arrays exhibiting a phase modulation range of 360° but nonideal amplitude characteristics, as shown in Figure 5c. The three different amplitude profiles represent distinct cases: constant amplitudes, linear functions, and Lorentzian line shapes. To obtain comparable results, the amplitude modulation of the two latter cases is chosen to be $A_{\text{mod}} = 20.0$. Figure 5d shows a comparison of the

directivity values obtained with forward and inverse designs for steering at $\theta_r = 15^\circ$. For constant amplitude, the directivity of both the forward- and inverse-designed arrays is ideal. Minor variations in the optimized directivity are attributed to the stochastic nature of the algorithm. In comparison, linearly varying amplitude leads to lower directivity. However, due to the assumed sigmoidal variation of phase, amplitudes vary minimally over a large segment of the phase modulation range. As a result, near-ideal performance can be attained with both forward and inverse design. In the case of the Lorentzian amplitude profile, however, the largest change in phase occurs precisely in the low amplitude regime. This introduces a considerable difference in the performance of forward and inverse designs. The forward-designed phase gradient profile relies on a constant phase shift between adjacent antennas. As a consequence, forward designs are highly sensitive to the antenna-specific amplitude profile and the directivity is reduced to $D_{\text{Lorentz,forward}} = 0.85 \times D_{\text{const,forward}}$. By contrast, the inverse-designed array is able to maintain considerably higher directivity with $D_{\text{Lorentz,inverse}} = 0.94 \times D_{\text{const,forward}}$. An

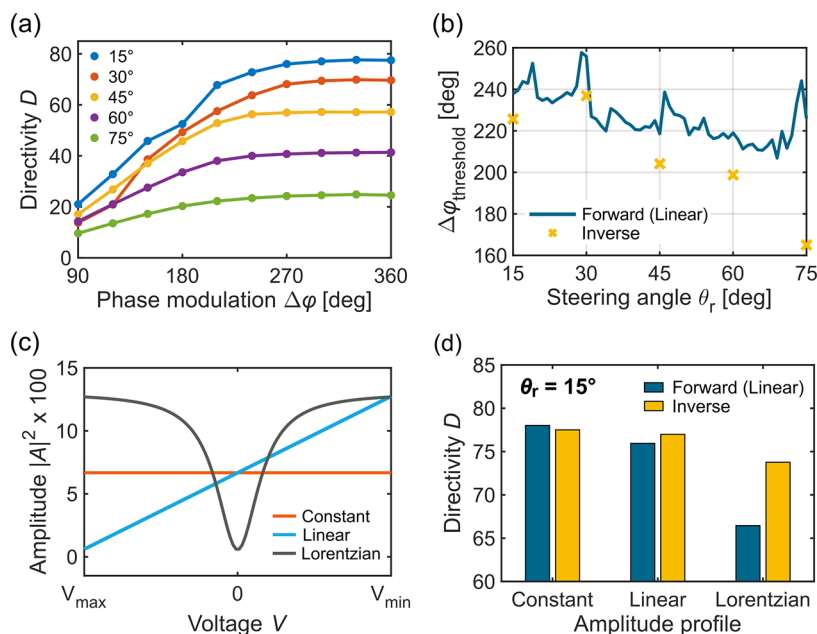


Figure 5. Analysis of a series of hypothetical structures consisting of a 1D array of 100 antennas uniformly spaced at 400 nm. The operating wavelength is $\lambda = 1550$ nm. (a) Optimized directivity D vs phase modulation range $\Delta\phi$ for a metasurface with constant amplitude $A = 1$. Optimized results are shown for steering at $\theta_r = 15^\circ$ (blue), 30° (orange), 45° (yellow), 60° (violet), 75° (green). (b) Required phase modulation $\Delta\phi_{\text{threshold}}$ for threshold directivity of $0.9 \times D_{\text{ideal}}(\theta_r)$ vs steering angle θ_r . Required phase modulation range is shown for forward (blue) and inverse designs (yellow). (c) Trial amplitude A as a function of the bias voltage V for three distinct cases: constant (orange), linear (blue), Lorentzian (gray). V_{min} and V_{max} are the minimal and maximal applied voltages, respectively. (d) Directivity D of forward-designed, linear phase profiles and inverse-designed arrays using amplitude relations shown in (c). The phase modulation corresponds to $\Delta\phi = 360^\circ$ and the steering angle is $\theta_r = 15^\circ$.

analysis of the optimized amplitude profile indicates that even though there is no significant difference in A_{mod} , inverse design adjusts the distribution of the phases across 360° such that there are considerably fewer antennas exhibiting low amplitude. As a result, sidelobes can be suppressed, increasing directivity (see Supporting Information Part 11 for an illustration of the optimized results). This study illustrates that array-scale inverse design is most beneficial for highly nonideal active metasurfaces that exhibit low amplitude under conditions of large phase shift. It is to be noted that such cases are typically reported in tunable structures that rely on intrinsic resonances. The results generated using array-level inverse design approach the ideal performance obtained for constant amplitude and a given phase modulation.

Experimental Validation of Array-Level Inverse Design. Here, we experimentally validate the array-level inverse design approach for an active beam steering metasurface. The previously introduced metasurface element (Figure 2a) is redesigned to ensure an operating wavelength of the fabricated metasurface around 1550 nm (Supporting Information Part 12). The resulting layer thicknesses are $t_b = 80$ nm, $t_{\text{alumina}} = 9.5$ nm, $t_{\text{ITO}} = 5$ nm, $t_h = 9.5$ nm, and $t_a = 40$ nm. The antenna and electrode dimensions are defined as $l_a = 210$ nm, $w_a = 160$ nm, and $w_e = 130$ nm, respectively, and the period is $d_x = 400$ nm. Additionally, we added a 60 nm thick silica (SiO₂) capping layer to increase device durability (Figure 6a). A scanning electron microscopy (SEM) image of the metasurface is shown in Figure 6b. We would like to note that the period of the metasurface postfabrication was measured to be $d_x = 430$ nm.

Once the metasurface was fabricated, we measured the spectra of the reflected light intensity (*i.e.*, reflectance) and

phase in order to characterize the tunable optical response of the metasurface under different applied biases. To do so, we measured the amplitude and phase of the reflected light using a tunable NIR laser in the wavelength range of 1420 nm – 1575 nm. The phase shift of the reflected light was determined using a Michelson interferometer in which interference fringe patterns were generated by the superposition of the beam reflected from the metasurface and the incident reference beam. The acquired phase shift was then extracted by fitting the interference fringe patterns to sinusoidal functions. The experimental setup and the procedure for phase and reflectance measurements is described in Supporting Information Part 13. The voltage-tunable optical response of the metasurface was then characterized by measuring the amplitude and phase of the reflection from the nanoantenna array while changing a bias voltage that was collectively applied to all antennas, resulting in a uniform change in phase across the metasurface. Figure 6c shows the experimentally measured reflectance as well as a total acquired phase shift of 223° for the light reflected from the fabricated metasurface. The operating wavelength was chosen to be $\lambda = 1548$ nm such that the phase shift provided by the metasurface could be maximized. Notably, considerably larger amplitudes than those reported in the full-wave simulation are obtained. This phenomenon has been observed previously^{27,30} and is attributed to a misalignment in the incident polarization. As the misaligned component of the incident light does not interact with the antenna, this effect leads to increased reflected intensity normal to the metasurface. Furthermore, since the misaligned component does not contribute to the accumulated phase shift, we assume reduced reflectance to approximate the actual amplitude contributing to the beam steering performance.

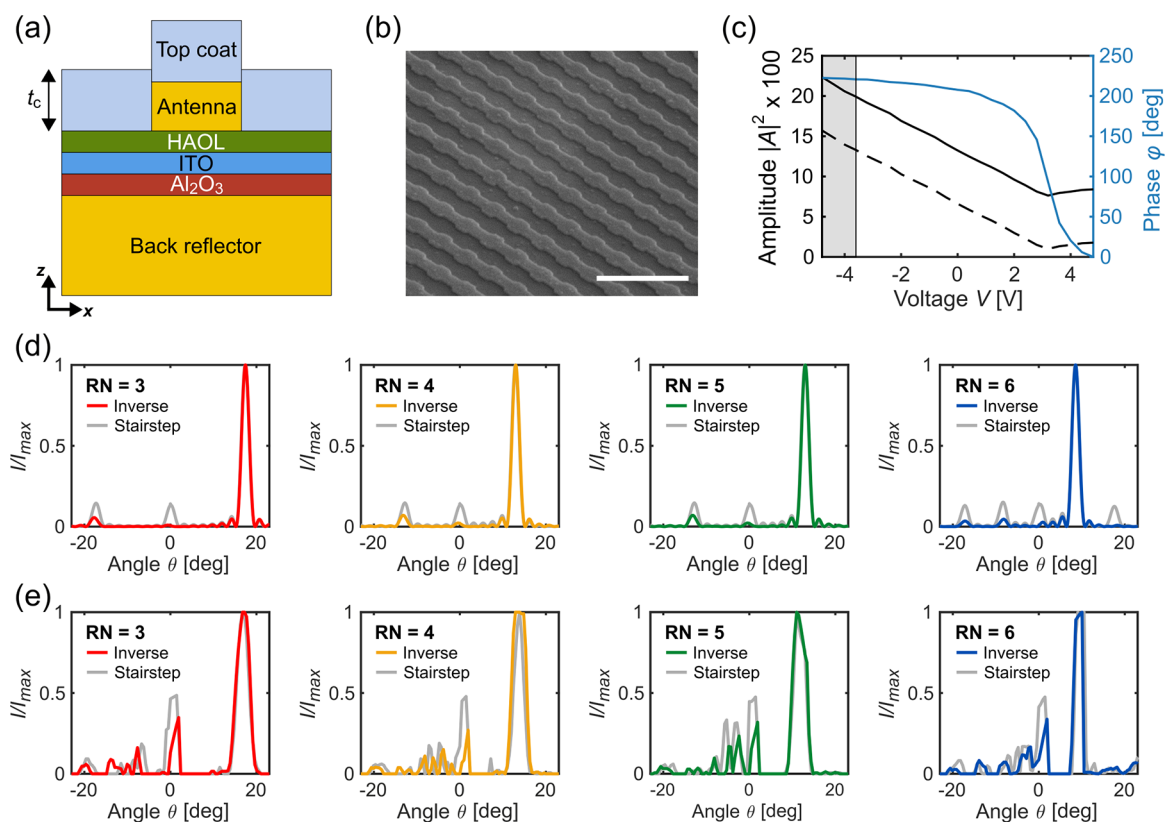


Figure 6. (a) Side-view schematic of the experimentally fabricated metasurface with a SiO_2 top-coat layer. The thickness of the coating layer is $t_c = 60$ nm. (b) Scanning electron microscopy (SEM) image of the fabricated nanoantennas with a scalebar of $1 \mu\text{m}$. (c) Measured phase shift (blue) and reflectance (black) as a function of the applied bias voltage. The dashed black line indicates the approximated reflectance contributing to the beam steering performance. Phase/amplitude values within the gray box were not used for optimization. (d) Analytically calculated and (e) experimentally measured far-field radiation patterns obtained using forward- (gray) and inverse-designed array profiles (colored). Forward designs are obtained using a four-level stairstep phase profile with repetition number (RN) varying from RN = 3 to 6 (left to right). All figures are plotted for the experimentally detectable angular range from -23° to $+23^\circ$.

Thus, a constant offset of $\Delta_r = 6.6\%$ is subtracted from the measured reflected light intensity (dashed black line in Figure 6c), leading to a minimum reflectance of 1%. The offset was accounted for in the array factor calculation by increasing the intensity at $\theta = 0^\circ$ by Δ_r . This approach was verified for previously measured far-field radiation patterns obtained using forward design,³⁰ as discussed in Supporting Information Part 14. Finally, an array-level optimization was performed using the measured phase shift and the actual approximated amplitude. Due to the difference between the work functions of Au and ITO, the ITO layer is slightly depleted at zero applied bias.²⁴ Thus, to avoid breakdown of the gate dielectric during beam steering measurements, we omit bias voltage applications below -3.6 V. Hence, a bias voltage range of $[-3.6$ V, $+4.8$ V] was used for the optimization, as indicated by the gray box in Figure 6c. As a result, a phase shift of $\Delta\varphi = 221^\circ$ was obtained. The optimized array phase and amplitude profiles are shown in Supporting Information Part 15. We note here that we confirmed through full-wave simulations of the forward- and inverse-designed array profiles that the fabricated reflectarray metasurface could be treated using the independent scatterer approximation (see Supporting Information Part 16), vindicating our approach to an array-level inverse design.

Figure 6d illustrates the analytically obtained beam steering performances using forward-designed four-level stairstep phase profiles with repetition numbers (RN) varying from RN = 3 to 6, as shown in Figure S18a. The far-field radiation patterns for

forward design are illustrated in gray. The corresponding beam steering radiation patterns obtained using array-level inverse design are overlaid in color in the respective figures. As can be seen, even though sidelobes are not entirely removed due to a reduced phase modulation along with operation at low amplitudes, a considerable sidelobe suppression that increases beam directivity is achieved (Table 1). We note that while the

Table 1. Analytically Computed vs Experimentally Measured Directivity D for $\theta = [-23^\circ, +23^\circ]$

directivity D	analytical, forward	analytical, inverse	experimental, forward	experimental, inverse
$\theta_r = 17.4^\circ$ (RN = 3)	16.1	19.8 (+23%)	8.7	9.7 (+11%)
$\theta_r = 12.9^\circ$ (RN = 4)	16.2	19.6 (+21%)	10.2	9.8 (−5%)
$\theta_r = 10.3^\circ$ (RN = 5)	13.9	18.3 (+32%)	8.4	9.6 (+15%)
$\theta_r = 8.5^\circ$ (RN = 6)	13.8	19.7 (+43%)	9.6	12.0 (+25%)

optimization was performed for the entire half-space (*i.e.*, additional sidelobes at larger polar angles were suppressed to increase directivity), we only visualize and evaluate the directivity for the experimentally detectable range from -23° to $+23^\circ$.

As a comparison, the experimental measurements for the beam steering active metasurface using forward- and inverse-

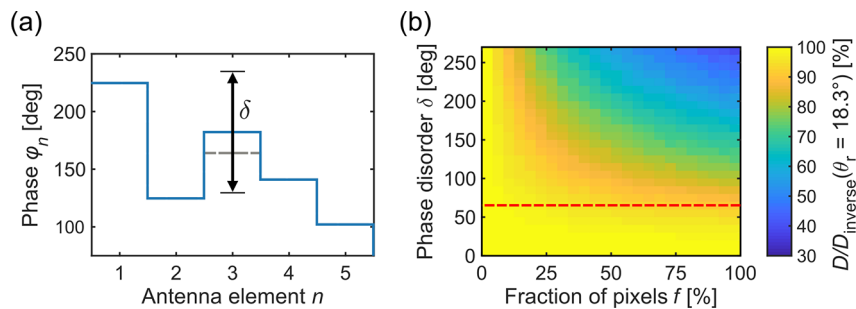


Figure 7. (a) Schematic for phase noise introduction in spatial phase profile. The phase disorder range δ is defined such that it allows distortion of each antenna phase by a uniformly distributed random phase value between 0° and $\pm \delta/2$. The schematic illustrates a phase disorder range of $\delta = 100^\circ$. The gray dashed line represents the disordered phase value. (b) Phase disorder range δ vs fraction of antennas f that are changed from their original value for the optimized array design illustrated in Figure 2e ($\theta_r = 18.3^\circ$). In the limiting case of $f = 100\%$, the inverse-designed array can tolerate up to $\pm 30^\circ$ phase error ($\delta = 60^\circ$) before going below $0.9 \times D_{\text{inverse}}$ (red dashed line). The data set is averaged over 100 implementations.

designed array profiles are illustrated in Figure 6e. Increased sidelobes as well as increased relative intensities compared to the analytically computed case, in particular for the specularly reflected light, are reported in both forward and inverse design. Notably, in the experiments conducted for staircase phase gradient profiles with repetition numbers varying from 3 to 6 (i.e., RN = 3, ..., 6), inverse design has resulted in an overall reduction in reflected optical power that is spuriously radiated outside the main steered beam, including specularly reflected power. The discrepancies in the amount of power radiated into undesired sidelobes between the analytical computations and experimental measurements are caused by the interplay of several effects, including antenna reflectances that are different from the assumed values, as well as a reduction in the available phase modulation range. Reduction in the achievable phase modulation range is caused by extrinsic damage from application of large bias voltages which results in a change in the leakage current as well as the breakdown field of the gate dielectric (Supporting Information Part 17). Since the fabricated metasurface operates around phase modulation values that are near the previously reported values of $\Delta\varphi_{\text{threshold}}$ (Figure 5b), further reduction in the phase modulation range can result in deviations of the beam steering performance from that analytically predicted using both forward- and inverse-designed array profiles. Furthermore, it should be noted that small variations in nanoantenna size can be introduced during metasurface fabrication. As a result, one can expect inconsistencies in amplitude and phase for individual scattering elements compared to the collectively measured optical response. Since the current experimental capability does not allow for an amplitude and phase measurement on a single-antenna basis, the notion of a phase/amplitude error becomes a crucial topic of discussion that is further investigated in the subsequent section. Notwithstanding the mentioned challenges, we were able to demonstrate experimentally that nonintuitive, inverse-designed array profiles can reduce spurious power coupled into sidelobes resulting from a nonoptimal metasurface phase and amplitude response, and this enhances the beam steering performance. For the measurements shown in Figure 6e, a maximal increase in directivity of 25% was obtained in comparison to the respective forward design for $\theta_r = 8.5^\circ$ (Table 1). In addition, inverse design decreased specular reflection by an average of 33%. We note that a broadening of the main lobe due to experimental angular resolution errors resulted in lower beam directivity for

$\theta_r = 12.9^\circ$ (RN = 4). Nonetheless, the peak sidelobe intensity was reduced by 43% in this case.

Beam Steering Arrays with Phase Disorder. The experimental realization of optimized, nonintuitive array designs is challenged by various sources of nonideality, error, and noise, such as discrepancies in actual phase and amplitude as a result of inconsistent nanoantenna sizes postfabrication, errors in bias application or interantenna coupling. The validity of the independent scatterer model was verified *via* full wave electromagnetic simulation for both forward and inverse designs in the case of the experimentally studied transparent conducting oxide reflectarray metasurface (Supporting Information Part 16). However, this fundamental assumption becomes nontrivial for alternative metasurface platforms exhibiting leaky resonant modes. As a consequence, the resulting deviation from the optimized phase and amplitude profiles are expected to cause additional scattering in undesired directions that lowers the directivity. Here, we perform a sensitivity analysis of the optimized designs to error and noise. To do this, we systematically introduce random phase noise and identify threshold values beyond which a strong decrease in directivity is observed. We characterize f as the fraction of antennas in the array differing from their original phase value $\varphi_{\text{original}}$. The phase disorder range δ further quantifies the maximal amount of phase error at each deviating element (Figure 7a). The disordered phase values $\varphi_{\text{disorder}}$ are calculated as

$$\varphi_{\text{disorder}} = \varphi_{\text{original}} + \text{rand}\left[-\frac{\delta}{2}, +\frac{\delta}{2}\right] \quad (6)$$

Here, $\text{rand}[x, y]$ computes a uniformly distributed random value between x and y . Capping of $\varphi_{\text{disorder}}$ at the minimal and maximal phase values ensures that upon adding phase noise, the antenna phase stays within the available phase modulation range. To account for the covarying amplitude and phase, $\varphi_{\text{disorder}}$ is additionally mapped to the corresponding amplitude, which is obtained from the antenna-specific optical response.

Figure 7b illustrates the error tolerance of an inverse-designed array phase profile for our example electro-optically tunable active metasurface steering at $\theta_r = 18.3^\circ$ (Figure 2e). The optimized array design is insensitive to small phase errors corresponding to small f and/or small δ . In the limiting case of $f = 100\%$, phase error is introduced into every antenna in the entire array. This case is characteristic of interantenna coupling that would lead to a distortion of the phase at each antenna

due to its nearest neighbors. Our analysis shows that optimized designs can tolerate up to $\pm 30^\circ$ phase error ($\delta = 60^\circ$) before reaching the directivity threshold of $0.9 \times D_{\text{inverse}}$. In comparison, forward design of nonideal active metasurfaces supports an increased threshold value of phase noise beyond $\delta = 100^\circ$ (see Supporting Information Part 18 for the error tolerance of forward designs in nonideal devices). The reduced error tolerance for inverse design is understandable, considering that our nonintuitive inverse-designed arrays typically exhibit more disordered phase profiles, even prior to any introduction of noise. As a result, they tolerate smaller errors before reaching substantial loss of information. Nonetheless, the findings reported in this analysis imply a considerable tolerance of phase noise for inverse-designed arrays.

CONCLUSION

In conclusion, we have developed a useful array-scale inverse design approach for active metasurface antenna arrays. Inverse design allows the array phase and amplitude profiles to be prescribed by change in the operating parameters of identical active antennas, rather than by geometrical shape optimization of individual antennas. We found that iterative optimization gives rise to nonintuitive array designs that enable high-directivity beam steering with nonideal antenna components. Specifically, for the electro-optically tunable metasurface analyzed in this work, directivities were enhanced by up to 84% compared to previously demonstrated forward designs. Sidelobe suppression approached ideal values. Near-ideal performance was demonstrated for continuous beam steering by optimization at angular increments of 0.5° . Inverse design reduced the required phase modulation range for high beam directivity. High-directivity beam steering was further reported for a phase modulation range as small as 180° . Furthermore, enhanced beam directivities using nonintuitive, inverse-designed array profiles were reported for an experimentally fabricated metasurface exhibiting a phase modulation of approximately 220° . Finally, a sensitivity analysis to antenna phase noise indicated that optimized designs could tolerate approximately $\pm 30^\circ$ phase error at each antenna without significant performance losses.

While the current work illustrates the power of an array-level inverse design on the beam steering performance in active metasurfaces, the same optimization framework can also be applied to a variety of alternative objective functions and active metasurface platforms. Similarly, a system-level optimization can also be performed for passive metasurfaces that rely on nonideal antenna components.⁵⁵

The results presented in this work constitute a compelling design approach for high performance in nonideal active metasurfaces. As an outlook, we expect that by combining array-level inverse design with optimization of individual antenna performance as well as optimization protocols applied to materials selection,^{56,57} a modern era for codesign of materials, device and system is arriving for nanophotonics. Ultimately, such an approach will enable the realization of highly efficient multifunctional metasurfaces capable of many functions beyond beam steering that allow complete space-time control of the scattered light wavefront.

METHODS

Full-Wave Simulation of Reconfigurable Metasurface. The full-wave electromagnetic simulation for the electro-optically tunable metasurface was performed using finite difference time domain optical

simulations (FDTD Lumerical). Here, a mesh size of 0.1 nm was used in the ITO layer. Moreover, we used 0.025 nm thick mesh sizes in the active regions of ITO (~ 2 nm thick) in order to carefully resolve the inhomogeneous permittivity profiles and capture the accurate optical response of the unit cell. The spatial distribution of the charge carriers in the ITO layer was calculated using finite element method (Device Lumerical). The scattered light amplitude and phase properties are extracted at the operating wavelength by simulating a periodic nanoantenna array biased at the desired voltage.

Genetic Optimization. The iterative genetic algorithm was implemented using the global optimization toolbox on MATLAB R2018b. A matrix containing the antenna-specific tunable phase-amplitude relation is provided as an input to the algorithm. Then a discrete integer optimization over the matrix rows (that define the scattered light response for various applied voltages) is performed with variable lower and upper bound defining the first and last row of the matrix, respectively. The default creation, crossover, and mutation functions of discrete genetic optimization enforce each variable to be an integer, as discussed in ref 58. To accommodate for the large number of parameters that are to be optimized, the population size is increased to 200. The optimized results are obtained with a crossover fraction of 0.95 and an elite count of 20. Each iteration stops when the average change in the best function value over 250 generations is less than 10^{-6} . The evolution of the iterative genetic optimization toward an optimal solution is illustrated in the supporting movie. Further details on the numerical framework can be found in Supporting Information Part 6.

Beam Steering Metasurface Device Fabrication. First, we clean silicon (Si) substrates with a 1 μm thick silica (SiO_2) layer on top using standard cleaning processes. Then the outermost parts of the connection pads are patterned using photolithography. After developing the exposed photoresist, we deposit a 20 nm thick titanium (Ti) layer followed by a 200 nm thick gold (Au) layer *via* e-beam evaporation. The excess resist and the Ti/Au film are removed through a lift-off process in acetone. Then, the Au back reflector is patterned using electron-beam lithography (EBL) [VISTEC EBPG 5000+] at an acceleration voltage of 100 keV after spinning an e-beam resist layer. The exposed e-beam resist layer is then developed and 3 nm of chromium (Cr) followed by an 80 nm-thick Au layer are deposited using an e-beam evaporator. In a next step, a 9.5 nm-thick alumina (Al_2O_3) layer is deposited on the samples through shadow mask *via* atomic layer deposition (ALD). Then, we pattern the ITO layer *via* EBL. Once the exposed resist is developed, we sputter a 5 nm thick ITO layer *via* room-temperature RF magnetron sputtering. The deposition pressure is 3 mTorr and the applied RF power is 48W. The plasma is struck by using argon (Ar) gas with a flow rate of 20 sccm, and argon/oxygen gas (Ar/O₂:90/10) with a tunable flow rate is used to control the carrier concentration of the deposited layer.²⁷ After lifting off the excess e-beam resist and films, the contact pads of the ITO layer are patterned *via* EBL followed by deposition of a Ti/Au film (20 nm/200 nm) using an e-beam evaporator. We then deposit the hafnium/aluminum oxide laminate (HAOL) gate dielectric layer through shadow masks by ALD.²⁷ In the next step, the nanoantennas as well as the inner contact lines are patterned on the sample using EBL. After developing the exposed e-beam resist, a 2 nm-thick germanium (Ge) layer followed by a 40 nm thick Au layer is deposited on the sample using an e-beam evaporator. Once the lift-off process is done, a 60 nm thick SiO_2 layer is deposited as the top coat through shadow mask *via* e-beam evaporation. Finally, 96 metasurface element pads and 4 ITO pads are wire-bonded from the sample to 100 conducting pads on a sample mounting printed circuit board (PCB) which itself is controlled by using a voltage-driving PCB.³⁰

ASSOCIATED CONTENT

Supporting Information

The Supporting Information is available free of charge at <https://pubs.acs.org/doi/10.1021/acsnano.0c05026>.

Independent scatterer model for subwavelength antenna arrays; phase gradient profiles; beam steering perform-

ance metrics: directivity vs power efficiency; complex dielectric permittivity of indium tin oxide (ITO); forward designs in nonideal antenna arrays; iterative genetic optimization: numerical framework; comparison to alternative optimization methods in terms of robustness; directivity and aperture size; target vs actual steering angle for continuous beam steering; phase modulations for analysis of hypothetical devices; optimized results for Lorentzian amplitude relations; full-wave simulation of experimentally demonstrated metasurface; experimental setup for phase and amplitude measurements; analytical model to account for experimental artifacts; forward- and inverse-designed array profiles for experimental metasurface; full-wave simulation of forward and inverse design for experimental metasurface array; change in phase modulation with consecutive measurements; error tolerance of forward designs in nonideal antenna arrays (PDF)

Evolution of the iterative genetic optimization toward an optimal solution (AVI)

AUTHOR INFORMATION

Corresponding Author

Harry A. Atwater — Thomas J. Watson Laboratory of Applied Physics, California Institute of Technology, Pasadena, California 91125, United States; orcid.org/0000-0001-9435-0201; Email: haa@caltech.edu

Authors

Prachi Thureja — Thomas J. Watson Laboratory of Applied Physics, California Institute of Technology, Pasadena, California 91125, United States; orcid.org/0000-0003-3852-3395

Ghazaleh Kafaie Shirmanesh — Thomas J. Watson Laboratory of Applied Physics, California Institute of Technology, Pasadena, California 91125, United States; orcid.org/0000-0003-1666-3215

Katherine T. Fountaine — NG Next, Northrop Grumman Corporation, Redondo Beach, California 90278, United States; orcid.org/0000-0002-0414-8227

Ruzan Sokhoyan — Thomas J. Watson Laboratory of Applied Physics, California Institute of Technology, Pasadena, California 91125, United States; orcid.org/0000-0003-4599-6350

Meir Grajower — Thomas J. Watson Laboratory of Applied Physics, California Institute of Technology, Pasadena, California 91125, United States; orcid.org/0000-0003-0726-8811

Complete contact information is available at: <https://pubs.acs.org/10.1021/acsnano.0c05026>

Author Contributions

§P.T. and G.K.S. contributed equally to this work.

Author Contributions

P.T., G.K.S., R.S., and H.A.A. conceived the original idea. P.T. analyzed forward design methods, designed the iterative genetic optimization, performed several optimization studies, analyzed the experimental results, and wrote the manuscript. G.K.S. and R.S. performed the design and simulations of the electro-optically tunable metasurface. G.K.S. performed the FDTD simulations and numerical design, fabricated the metasurface device, performed the optical measurements, and extracted the experimental data. K.T.F. helped with the analysis of forward design methods and the design of the genetic algorithm. R.S. and M.G. supported in designing theoretical

studies and performing data analysis. G.K.S. and M.G. built the experimental setup. H.A.A. organized the project, designed optimization studies, analyzed the results, and prepared the manuscript. All authors have given approval to the final version of the manuscript.

Funding

This work was supported by National Aeronautics and Space Administration (NASA) Early Stage Innovation (ESI) Grant 80NSSC19K0213 and Samsung Electronics.

Notes

The authors declare no competing financial interest.

ACKNOWLEDGMENTS

The authors thank L. Sweatlock and P. Hon regarding preliminary discussions about the project and Y. Tokpanov for discussions regarding optimization algorithms. The authors acknowledge metasurface device fabrication support provided by the Kavli Nanoscience Institute (KNI). The FDTD computations presented here were conducted on the Caltech High Performance Cluster, partially supported by a grant from the Gordon and Betty Moore Foundation.

REFERENCES

- (1) Schwarz, B. Lidar: Mapping the World in 3D. *Nat. Photonics* **2010**, *4*, 429–430.
- (2) Feng, F.; White, I. H.; Wilkinson, T. D. Free Space Communications with Beam Steering a Two-Electrode Tapered Laser Diode Using Liquid-Crystal SLM. *J. Lightwave Technol.* **2013**, *31*, 2001–2007.
- (3) Yu, N.; Genevet, P.; Aieta, F.; Kats, M. A.; Blanchard, R.; Aoust, G.; Tetienne, J.-P.; Gaburro, Z.; Capasso, F. Flat Optics: Controlling Wavefronts with Optical Antenna Metasurfaces. *IEEE J. Sel. Top. Quantum Electron.* **2013**, *19*, 4700423–4700423.
- (4) Yaacobi, A.; Sun, J.; Moresco, M.; Leake, G.; Coolbaugh, D.; Watts, M. R. Integrated Phased Array for Wide-Angle Beam Steering. *Opt. Lett.* **2014**, *39*, 4575–4578.
- (5) Doylend, J. K.; Heck, M. J. R.; Bovington, J. T.; Peters, J. D.; Coldren, L. A.; Bowers, J. E. Two-Dimensional Free-Space Beam Steering with an Optical Phased Array on Silicon-on-Insulator. *Opt. Express* **2011**, *19*, 21595–21604.
- (6) Sun, J.; Timurdogan, E.; Watts, M. R.; Hosseini, E. S.; Yaacobi, A. Large-Scale Nanophotonic Phased Array. *Nature* **2013**, *493*, 195–199.
- (7) Yoo, B.-W.; Megens, M.; Chan, T.; Sun, T.; Yang, W.; Chang-Hasnian, C. J.; Horsley, D. A.; Wu, M. C. Optical Phased Array Using High Contrast Gratings for Two Dimensional Beamforming and Beamsteering. *Opt. Express* **2013**, *21*, 12238–12248.
- (8) Yoo, B.-W.; Megens, M.; Sun, T.; Yang, W.; Chang-Hasnian, C. J.; Horsley, D. A.; Wu, M. C. A 32×32 Optical Phased Array Using Polysilicon Sub-Wavelength High-Contrast-Grating Mirrors. *Opt. Express* **2014**, *22*, 19029–19039.
- (9) Chan, T. K.; Megens, M.; Yoo, B.-W.; Wyras, J.; Chang-Hasnian, C. J.; Wu, M. C.; Horsley, D. A. Optical Beamsteering Using an 8×8 MEMS Phased Array with Closed-Loop Interferometric Phase Control. *Opt. Express* **2013**, *21*, 2807–2815.
- (10) Aflatouni, F.; Abiri, B.; Rekh, A.; Hajimiri, A. Nanophotonic Projection System. *Opt. Express* **2015**, *23*, 21012–21022.
- (11) Zadka, M.; Chang, Y.-C.; Mohanty, A.; Phare, C. T.; Roberts, S. P.; Lipson, M. On-Chip Platform for a Phased Array with Minimal Beam Divergence and Wide Field-of-View. *Opt. Express* **2018**, *26*, 2528–2534.
- (12) Hutchison, D. N.; Sun, J.; Doylend, J. K.; Kumar, R.; Heck, J.; Kim, W.; Phare, C. T.; Feshali, A.; Rong, H. High-Resolution Aliasing-Free Optical Beam Steering. *Optica* **2016**, *3*, 8–11.

- (13) Fatemi, R.; Khachaturian, A.; Hajimiri, A. A Nonuniform Sparse 2-D Large-FOV Optical Phased Array with a Low-Power PWM Drive. *IEEE J. Solid-State Circuits* **2019**, *54*, 1200–1215.
- (14) Yu, N.; Genevet, P.; Kats, M. A.; Aieta, F.; Tietienne, J.-P.; Capasso, F.; Gaburro, Z. Light Propagation with Phase Discontinuities: Generalized Laws of Reflection and Refraction. *Science* **2011**, *334*, 333–337.
- (15) Kildishev, A. V.; Boltasseva, A.; Shalaev, V. M. Planar Photonics with Metasurfaces. *Science* **2013**, *339*, 1232009.
- (16) Farmahini-Farahani, M.; Mosallaei, H. Birefringent Reflectarray Metasurface for Beam Engineering in Infrared. *Opt. Lett.* **2013**, *38*, 462–464.
- (17) Lin, D.; Fan, P.; Hasman, E.; Brongersma, M. L. Dielectric Gradient Metasurface Optical Elements. *Science* **2014**, *345*, 298–302.
- (18) Shalaev, M. I.; Sun, J.; Tsukernik, A.; Pandey, A.; Nikolskiy, K.; Litchinitser, N. M. High-Efficiency All-Dielectric Metasurfaces for Ultracompact Beam Manipulation in Transmission Mode. *Nano Lett.* **2015**, *15*, 6261–6266.
- (19) Wang, J.; Hou, P.; Cai, H.; Sun, J.; Wang, S.; Wang, L.; Yang, F. Continuous Angle Steering of an Optically-Controlled Phased Array Antenna Based on Differential True Time Delay Constituted by Micro-Optical Components. *Opt. Express* **2015**, *23*, 9432–9439.
- (20) Balanis, C. A. *Antenna Theory: Analysis and Design*; Wiley: Hoboken, 2016.
- (21) Visser, H. J. *Array and Phased Array Antenna Basics*; Wiley: Hoboken, 2005.
- (22) Engström, D.; Bengtsson, J.; Eriksson, E.; Goksör, M. Improved Beam Steering Accuracy of a Single Beam with a 1D Phase-Only Spatial Light Modulator. *Opt. Express* **2008**, *16*, 18275–18287.
- (23) Shaltout, A. M.; Shalaev, V. M.; Brongersma, M. L. Spatiotemporal Light Control with Active Metasurfaces. *Science* **2019**, *364*, No. eaat3100.
- (24) Huang, Y. W.; Lee, H. W. H.; Sokhoyan, R.; Pala, R. A.; Thyagarajan, K.; Han, S.; Tsai, D. P.; Atwater, H. A. Gate-Tunable Conducting Oxide Metasurfaces. *Nano Lett.* **2016**, *16*, 5319–5325.
- (25) Park, J.; Kang, J. H.; Kim, S. J.; Liu, X.; Brongersma, M. L. Dynamic Reflection Phase and Polarization Control in Metasurfaces. *Nano Lett.* **2017**, *17*, 407–413.
- (26) Sherrott, M. C.; Hon, P. W. C.; Fountaine, K. T.; Garcia, J. C.; Ponti, S. M.; Brar, V. W.; Sweatlock, L. A.; Atwater, H. A. Experimental Demonstration of $> 230^\circ$ Phase Modulation in Gate-Tunable Graphene-Gold Reconfigurable Mid-Infrared Metasurfaces. *Nano Lett.* **2017**, *17*, 3027–3034.
- (27) Kafaie Shirmanesh, G.; Sokhoyan, R.; Pala, R. A.; Atwater, H. A. Dual-Gated Active Metasurface at 1550 nm with Wide ($>300^\circ$) Phase Tunability. *Nano Lett.* **2018**, *18*, 2957–2963.
- (28) Kim, Y.; Wu, P. C.; Sokhoyan, R.; Mauser, K.; Glauddell, R.; Kafaie Shirmanesh, G.; Atwater, H. A. Phase Modulation with Electrically Tunable Vanadium Dioxide Phase-Change Metasurfaces. *Nano Lett.* **2019**, *19*, 3961–3968.
- (29) Wu, P. C.; Pala, R. A.; Kafaie Shirmanesh, G.; Cheng, W.; Sokhoyan, R.; Grajower, M.; Alam, M. Z.; Lee, D.; Atwater, H. A. Dynamic Beam Steering with All-Dielectric Electro-Optic III-V Multiple-Quantum-Well Metasurfaces. *Nat. Commun.* **2019**, *10*, 1–9.
- (30) Shirmanesh, G. K.; Sokhoyan, R.; Wu, P. C.; Atwater, H. A. Electro-Optically Tunable Multifunctional Metasurfaces. *ACS Nano* **2020**, *14*, 6912–6920.
- (31) Kats, M. A.; Sharma, D.; Lin, J.; Genevet, P.; Blanchard, R.; Yang, Z.; Qazilbash, M. M.; Basov, D. N.; Ramanathan, S.; Capasso, F. Ultra-Thin Perfect Absorber Employing a Tunable Phase Change Material. *Appl. Phys. Lett.* **2012**, *101*, 221101.
- (32) He, J.; Xie, Z.; Sun, W.; Wang, X.; Ji, Y.; Wang, S.; Lin, Y.; Zhang, Y. Terahertz Tunable Metasurface Lens Based on Vanadium Dioxide Phase Transition. *Plasmonics* **2016**, *11*, 1285–1290.
- (33) Ou, J. Y.; Plum, E.; Jiang, L.; Zheludev, N. I. Reconfigurable Photonic Metamaterials. *Nano Lett.* **2011**, *11*, 2142–2144.
- (34) Holsteen, A. L.; Raza, S.; Fan, P.; Kik, P. G.; Brongersma, M. L. Purcell Effect for Active Tuning of Light Scattering from Semiconductor Optical Antennas. *Science* **2017**, *358*, 1407–1410.
- (35) Arbabi, E.; Arbabi, A.; Kamali, S. M.; Horie, Y.; Faraji-Dana, M.; Faraon, A. MEMS-Tunable Dielectric Metasurface Lens. *Nat. Commun.* **2018**, *9*, 1–9.
- (36) Han, S.; Kim, S.; Kim, S.; Low, T.; Brar, V. W.; Jang, M. S. Complete Complex Amplitude Modulation with Electronically Tunable Graphene Plasmonic Metamolecules. *ACS Nano* **2020**, *14*, 1166–1175.
- (37) Piggott, A. Y.; Lu, J.; Lagoudakis, K. G.; Petykiewicz, J.; Babinec, T. M.; Vucković, J. Inverse Design and Demonstration of a Compact and Broadband On-Chip Wavelength Demultiplexer. *Nat. Photonics* **2015**, *9*, 374–377.
- (38) Sell, D.; Yang, J.; Doshay, S.; Yang, R.; Fan, J. A. Large-Angle, Multifunctional Metagratings Based on Freeform Multimode Geometries. *Nano Lett.* **2017**, *17*, 3752–3757.
- (39) Pestourie, R.; Pérez-Arancibia, C.; Lin, Z.; Shin, W.; Capasso, F.; Johnson, S. G. Inverse Design of Large-Area Metasurfaces. *Opt. Express* **2018**, *26*, 33732–33747.
- (40) Molesky, S.; Lin, Z.; Piggott, A. Y.; Jin, W.; Vucković, J.; Rodriguez, A. W. Inverse Design in Nanophotonics. *Nat. Photonics* **2018**, *12*, 659–670.
- (41) Jafar-Zanjani, S.; Inampudi, S.; Mosallaei, H. Adaptive Genetic Algorithm for Optical Metasurfaces Design. *Sci. Rep.* **2018**, *8*, 1–16.
- (42) Inampudi, S.; Mosallaei, H. Neural Network Based Design of Metagratings. *Appl. Phys. Lett.* **2018**, *112*, 241102.
- (43) Kudyshev, Z. A.; Kildishev, A. V.; Shalaev, V. M.; Boltasseva, A. Machine-Learning-Assisted Metasurface Design for High-Efficiency Thermal Emitter Optimization. *Appl. Phys. Rev.* **2020**, *7*, 021407.
- (44) Egorov, V.; Eitan, M.; Scheuer, J. Genetically Optimized All-Dielectric Metasurfaces. *Opt. Express* **2017**, *25*, 2583–2593.
- (45) Jiang, J.; Fan, J. A. Global Optimization of Dielectric Metasurfaces Using a Physics-Driven Neural Network. *Nano Lett.* **2019**, *19*, 5366–5372.
- (46) Elsayy, M. M. R.; Lanteri, S.; Duvigneau, R.; Brière, G.; Mohamed, M. S.; Genevet, P. Global Optimization of Metasurface Designs Using Statistical Learning Methods. *Sci. Rep.* **2019**, *9*, 1–15.
- (47) Chung, H.; Miller, O. D. Tunable Metasurface Inverse Design for 80% Switching Efficiencies and 144° Angular Deflection. *ACS Photonics* **2020**, *7*, 2236–2243.
- (48) Li, S. Q.; Xu, X.; Veetil, R. M.; Valuckas, V.; Paniagua-Domínguez, R.; Kuznetsov, A. I. Phase-Only Transmissive Spatial Light Modulator Based on Tunable Dielectric Metasurface. *Science* **2019**, *364*, 1087–1090.
- (49) Hansen, R. C. *Phased Array Antennas*; Wiley: Hoboken, 1998.
- (50) Feigenbaum, E.; Diest, K.; Atwater, H. A. Unity-Order Index Change in Transparent Conducting Oxides at Visible Frequencies. *Nano Lett.* **2010**, *10*, 2111–2116.
- (51) Dionne, J. A.; Diest, K.; Sweatlock, L. A.; Atwater, H. A. PlasMOSstor: A Metal-Oxide-Si Field Effect Plasmonic Modulator. *Nano Lett.* **2009**, *9*, 897–902.
- (52) Forouzmmand, A.; Salary, M. M.; Kafaie Shirmanesh, G.; Sokhoyan, R.; Atwater, H. A.; Mosallaei, H. Tunable All-Dielectric Metasurface for Phase Modulation of the Reflected and Transmitted Light via Permittivity Tuning of Indium Tin Oxide. *Nanophotonics* **2019**, *8*, 415–427.
- (53) Goldberg, D. E. *Genetic Algorithms*; Pearson Education: New York, 2006.
- (54) Johnson, J. M.; Rahmat-Samii, Y. Genetic Algorithms in Engineering Electromagnetics. *IEEE Antennas Propag. Mag.* **1997**, *39*, 7–21.
- (55) Fan, Y.; Xu, Y.; Qiu, M.; Jin, W.; Zhang, L.; Lam, E. Y.; Tsai, D. P.; Lei, D. Phase-Controlled Metasurface Design via Optimized Genetic Algorithm. *Nanophotonics* **2020**, *9*, 3931–3939.
- (56) Sanchez-Lengeling, B.; Aspuru-Guzik, A. Inverse Molecular Design Using Machine Learning: Generative Models for Matter Engineering. *Science* **2018**, *361*, 360–365.
- (57) Zunger, A. Inverse Design in Search of Materials with Target Functionalities. *Nat. Rev. Chem.* **2018**, *2*, 1–16.

(58) Deep, K.; Singh, K. P.; Kansal, M. L.; Mohan, C. A Real Coded Genetic Algorithm for Solving Integer and Mixed Integer Optimization Problems. *Appl. Math. Comput.* **2009**, *212*, 505–518.